

A Numerical Study of Taylor Bubbles

Xiaozhen Lu and Andrea Prosperetti*

Department of Mechanical Engineering, Johns Hopkins University, Baltimore, Maryland 21218

Some results of a computational study of axisymmetric Taylor bubbles rising in a vertical tube filled with a quiescent, upward- or downward-flowing liquid are presented. The computational method is based on a finite-volume discretization of the Navier–Stokes equations on a staggered grid. The interface is maintained sharp and is discretized using a set of marker points linked by cubic splines. Independent theoretical results and published data are used for its validation. The simulations illustrate the effect of the Morton and Eötvös numbers on several steady-state and time-dependent processes.

Introduction

Vertical slug flow is encountered in a variety of industrial applications such as geothermal energy production, oil extraction, steam generators, and others. In this flow regime, liquid “slugs” are separated by large bullet-shaped gas or vapor bubbles, the so-called Taylor bubbles, with a diameter close to that of the conduit and a length of several conduit diameters. There is a substantial body of experimental literature dealing with flow of this type (e.g., see refs 1 and 2), while theoretical understanding is more limited. Some progress on the mechanics of single Taylor bubbles has been made based on simplified models, which, however, as recently stressed by Funada et al.,³ still leave many features of this flow unexplained. Much more remains to be understood concerning, for example, the mutual interaction among bubbles, the mechanisms that control their spacing, their size, and others. The complexity of the flow is such that further theoretical progress requires a greater insight into its properties. Although experiment is, of course, a prime source of insight, computation is also a promising avenue of investigation, and it is this avenue that we pursue in this paper.

Full Navier–Stokes computational investigations of slug flow have a perhaps surprisingly short history. The earliest paper appears to be the study by Mao and Dukler,⁴ which simulated steady single bubbles by a cut-cell, finite-difference method. They focused on the numerical method and the issue of uniqueness of the solution, and they only presented limited results. Tomiyama, Sou, and Sakaguchi⁵ used a volume-of-fluid method to calculate the flow field both inside and outside the bubble. Their interest was in single, relatively short bubbles rising in standing liquids of moderate to high viscosity; the maximum Reynolds number based on the bubble rise velocity was less than 90. Bugg, Mack, and Rezkallah⁶ and Bugg and Saad⁷ presented detailed results on the velocity distribution in the liquid ahead of, behind, and along the sides of single Taylor bubbles. They used a volume-of-fluid method, sharing with the one described later the idea of extrapolating one variable—pressure in their case, velocity in ours—from the liquid phase into the gas phase. They considered a range of physical properties with Eötvös numbers (Eu) between 10 and 100 and Morton numbers (Mo) between 10^{-12} and 10. Son⁸ described a level-set numerical method to examine free surface flows and illustrated it with an application to a periodic train of Taylor bubbles. Anglart and Podowski⁹ conducted the first three-dimensional simulation of interacting Taylor bubbles. They simulated the coalescence

between two bubbles and found that, although the leading bubble maintains an axial symmetry, the trailing bubble becomes distorted before merging with the leading one. In all of the previous papers, the flow was laminar. Very recently, Taha and Cui¹⁰ presented fully three-dimensional numerical results that were calculated including a turbulence model. They were able to confirm several of the experimental observations available in the literature.

Mathematical Model and Computational Method

We simulate flow in a vertical tube by solving the standard incompressible Navier–Stokes equations under the assumption of axial symmetry. The no-slip condition is applied at the tube wall. On the surface of the bubble, the tangential stress vanishes and the difference in normal stresses is balanced by the effect of surface tension:

$$p = p_g - \sigma \kappa + \mu \mathbf{n} \cdot (\nabla \mathbf{v} + \nabla \mathbf{v}^T) \cdot \mathbf{n} \quad (1)$$

Here p and \mathbf{v} are the liquid pressure and velocity, μ is the liquid viscosity, σ is the surface tension coefficient, κ is the local curvature, and \mathbf{n} is the unit normal to the interface. We neglect the flow in the gas, representing its dynamical effects simply by a spatially uniform pressure p_g ; we also neglect the gas density in comparison with that of the liquid.

In many of the examples shown in this paper, the situation is schematized as a train of identical bubbles separated by a constant distance L and distributed in space along the length of the tube (see, e.g., the work of Wallis¹¹). In view of this spatial periodicity, it is thus sufficient to limit the computational domain to a single cell, i.e., a portion of tube of length L . The velocity field at the top of the domain (at $z = L$) is taken to be an exact replica of that at the bottom (at $z = 0$), while the pressure field differs by a constant from cell to cell, according to $p(0, r) = p(L, r) + \Delta P$, in which ΔP is a constant. In some cases, ΔP will be prescribed, whereas, in others, it will be adjusted to have a prescribed mean liquid flow in the tube:

$$2\pi \int_0^{D/2} v_z r \, dr = \frac{\pi}{4} D^2 \bar{U} \quad (2)$$

Here, v_z is the velocity component in the direction of the tube axis, \bar{U} the total volumetric flux (equal to the cross-sectional averaged liquid velocity away from the bubble), and D the diameter of the tube.

The numerical method is a modification of that developed by Popinet and Zaleski,¹² to whose paper the reader is referred for details (see also ref 13). The full incompressible axisym-

* To whom correspondence should be addressed. Tel.: (+1-410) 516 8534. Fax: (+1-410) 516 7254. E-mail address: prosperetti@jhu.edu.

metric Navier–Stokes equations are solved by a pressure correction method with first-order time accuracy on a staggered mesh. The pressure calculation is cast in terms of a pressure increment which is substituted into the continuity equation to obtain a Poisson equation, which is solved using the biconjugate gradient method.¹⁴ Ghost cells are used to impose the correct boundary conditions on the axis and the tube wall.

To simplify the computational procedure, the interface is prevented from crossing the top or bottom boundaries in the following way. Before starting the time-stepping procedure to advance the solution from t^n to t^{n+1} , the bubble nose velocity (V_B^n) is subtracted from all the vertical velocity components and $-V_B^n$ is prescribed as a boundary condition on the wall. The time stepping is then executed by finding a new relative velocity \tilde{v}_z^{n+1} , which is converted back to the fixed-frame velocity by adding the nose velocity that had been subtracted:

$$v_z^{n+1} = \tilde{v}_z^{n+1} + V_B^n$$

For the next time step, the nose velocity updated in this way is used, and so on. With this device, the nose position changes little over the course of the calculation, which is effectively always performed in the fixed frame, because the correct accelerations ($\tilde{v}_z^{n+1} + V_B^n$) – ($\tilde{v}_z^n + V_B^{n-1}$) are always used.

The interface is discretized using a set of marker points linked by cubic splines. This description supplies an accurate knowledge of the position and curvature of the interface necessary to evaluate the surface tension contribution. The marker points are convected according to the local velocity of the liquid. At the end of each time step, they are uniformly redistributed to ensure that the distance between two consecutive marker points does not exceed 90% of the grid size.

In the method described by Popinet and Zaleski,¹² velocities on the gas side of the interface are needed for the discretization, and the velocity and its gradient on the interface are also needed to transport the marker points and to impose the boundary condition described by eq 1. We have implemented a procedure based on B-splines to provide a cubic extrapolation (see, for example, ref 15), based on the computed liquid points within three mesh spacings from the interface. This procedure permits one to construct smooth functions best-fitting the field variables over a strip straddling the interface along its entire perimeter. These functions are used to evaluate the velocity components and their gradients in the interfacial region as needed (see ref 13 for details).

Validation

We illustrate the accuracy of the code with two validation tests: the volume oscillations of a spherical bubble immersed in an incompressible liquid and a Taylor bubble rising in a stagnant moderately viscous liquid.

The dynamics of a spherical bubble in an incompressible liquid is governed by the Rayleigh–Plesset equation (see, e.g., ref 16):

$$R\ddot{R} + \frac{3}{2}\dot{R}^2 = \frac{1}{\rho} \left[p_g - p_\infty - \frac{2\sigma}{R} - 4\mu \left(\frac{\dot{R}}{R} \right) \right] \quad (3)$$

where R is the bubble radius, p_g the pressure inside the bubble, and p_∞ the ambient pressure. For the present validation purposes, a simple isothermal model for the internal pressure is sufficient; we take $p_g = (R_0/R)^3 p_{g0}$, where the subscript “0” indicates initial values. The bubble is centered at the center of the computational domain, which is taken as a cylinder with a height of $24R_0$ and a radius of $12R_0$; a constant pressure p_∞ is applied on the outer

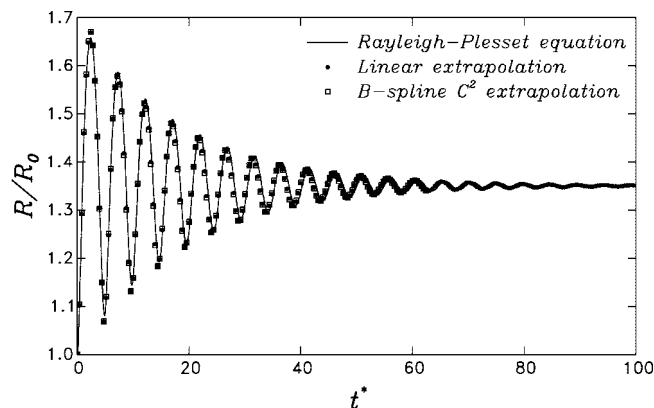


Figure 1. Damped radial oscillations of a spherical bubble in a viscous liquid. The continuous line is the result calculated from the Rayleigh–Plesset equation (described by eq 3), whereas the points and squares have been obtained with the present method, using linear and B-spline extrapolation, respectively. The dimensionless time is defined as $t^* = t/[R_0(\rho/P_\infty)^{1/2}]$.

boundary, where the normal derivatives of the velocity components are set to zero. The discretization used 150 and 300 cells in the radial and axial directions, respectively.

Figure 1 shows the radius of the bubble, as given by our code, compared with the solution of eq 3. The characteristic length and time scales are taken as the initial radius R_0 and $R_0(\rho/P_\infty)^{1/2}$. In nondimensional form, the pertinent quantities have the following values: $R(0)/R_0 = 1$, $p_{g0}/p_\infty = 2.5$, $\sigma/(R_0 p_\infty) = 0.01$, $\mu/[R_0(\rho p_\infty)^{1/2}] = 0.05$. For $p_\infty = 101.3$ kPa, these numerical values would correspond to a bubble with a radius of ~ 70 μm in a 58% sucrose solution with the properties shown in Table 1.

We found that linear velocity extrapolation gives essentially indistinguishable results from the B-splines extrapolation, as far as velocities are concerned; however, when velocity gradients are compared, some differences appear. An example is shown in Figure 2, which shows $\partial v_r / \partial z$ along the bubble surface; here, the horizontal axis is the arc length along the interface normalized by R_0 .

The B-spline extrapolation shows excellent agreement with the exact solution, whereas the linear extrapolation is less satisfactory. However, the computational time increases by a factor of ~ 8 . For this reason, we have used this high-accuracy extrapolation only in a few cases in which the bubble surface was sufficiently complex that high accuracy seemed to be warranted. At the beginning of this study, we ran several comparisons between the two methods for many cases in which the bubble surface was smooth, finding negligible differences.

Bugg and Saad⁷ made PIV measurements of the velocity field around a rising Taylor bubble in a 19-mm-diameter tube that contained stagnant olive oil, with a density of 911 kg/m^3 and a viscosity of 84 cP; the surface tension was 0.0328 N/m. The corresponding values of the Morton and Eötvös numbers, which are defined as

$$Mo = \frac{g\mu^4}{\rho\sigma^3} \quad (4a)$$

and

$$Eo = \frac{\rho g D^2}{\sigma} \quad (4b)$$

were 0.015 and 100, respectively. To simulate this case, we used linear extrapolation. The computational domain had a length of 8 tube diameters and was discretized with square cells

Table 1. Representative Liquids and Tube Diameters Corresponding to the Morton (Mo) and Eötvös (Eo) Numbers Used in the Present Numerical Examples^a

fluid	Morton number, Mo	tube diameter, D (mm)	Eötvös number, Eo	$U_B/(gD)^{1/2}$
distilled water	1.6×10^{-11}	10	14.7	0.24
distilled water	1.6×10^{-11}	15	33	0.32
40% sucrose solution	1.8×10^{-8}	10	0.23	
40% sucrose solution	1.8×10^{-8}	20	60	0.33
58% sucrose solution	4.7×10^{-5}	10	16.4	0.19
90% glycerol solution	1.6×10^{-2}	10	18.7	0.10
90% glycerol solution	1.6×10^{-2}	20	74.6	0.27

^a $Mo = g\mu^4/(\rho\sigma^3)$, and $Eo = \rho g D^2/\sigma$. The last column shows the computed dimensionless bubble rising velocity, which is within 1% of the values measured by White and Beardmore.¹⁸

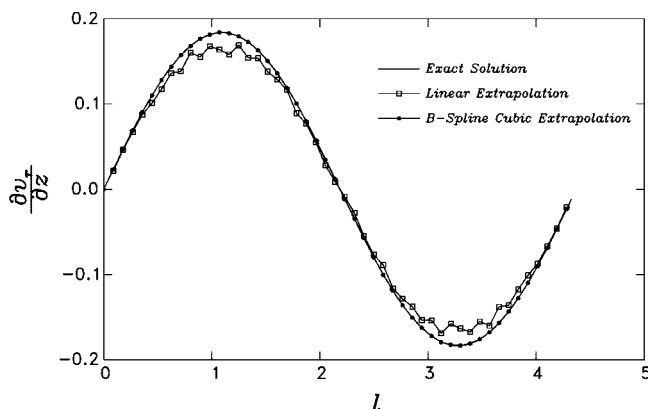


Figure 2. Velocity gradient $\partial v_z/\partial z$ along the surface of the oscillating spherical bubble of the previous figure at $t^* = 16$. The continuous line is the exact analytical result; the points and squares have been obtained with the present method, using linear and B-spline extrapolation, respectively. The horizontal axis is the arc length along the interface normalized by R_0 .

with 35 equally spaced nodes in the radial direction. For the velocity, the boundary condition described by eq 2, with $\bar{U} = 0$, was used. The terminal rising velocity was measured to be $U_B/(gD)^{1/2} = 0.299$, whereas our code gave a value of 0.303, which is a difference of slightly more than 1%.

Figure 3 shows the axial velocity along the tube axis above the bubble, as a function of the distance from the bubble nose at $z = 0$. Figure 4 shows the axial and radial velocity components at a distance of $z/D = 0.111$ above the bubble, as a function of the distance from the axis. The numerical results show very satisfactory agreement with these PIV measurements.

Below the bubble nose, at $z/D = -0.504$, a falling film begins to develop (see Figure 5) and becomes fully developed further down (see Figure 6, at $z/D = -2.34$). Our numerical simulation predicts the location of the gas/liquid interface for this fully developed film region at $r/R = 0.76$, which agrees well with the value of 0.75 that is given by the analysis from ref 17 and the numerical prediction of 0.76 that is obtained from ref 7.

Figure 7 shows the velocity field in the wake of the Taylor bubble at a distance of $1/5D$ below the bubble tail. The radial component of the velocity is well-predicted by the numerical simulation, whereas the axial component is slightly underpredicted. This underprediction is also found in the numerical calculation of Bugg and Saad.⁷ These authors explain it as likely due to the fact that the bottom edge of the bubble is not as rounded in the prediction as it is in the experiments. This affects the way in which the falling film interacts with the fluid below the bubble. On the other hand, given that two independent calculations—the present one and that Bugg and Saad⁷—both show the same difference with the data, it could well be that the data are slightly inaccurate in this region.

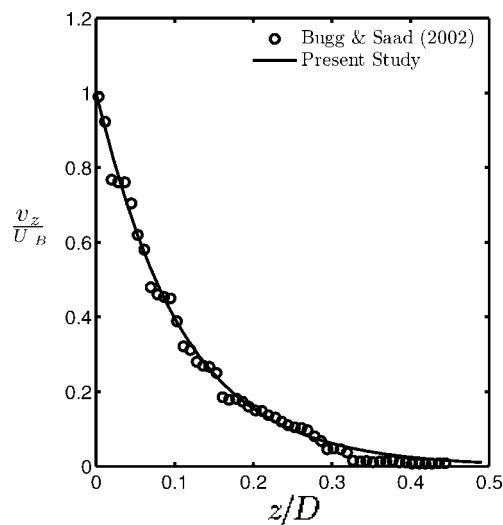


Figure 3. Axial component of velocity along the tube axis above the bubble; the numerical results (solid line) are compared to the PIV measurements from Bugg and Saad.⁷

In conclusion, both validation tests suggest that the present numerical method and its computational implementation exhibit a satisfactory degree of accuracy and can be used to explore several features of the phenomenon under consideration.

Rise in a Stagnant Liquid

Table 1 shows the Mo and Eo values that we consider in the examples that follow, and the table includes examples of liquids and tube diameters that would produce these dimensionless values. These same property values were considered by White and Beardmore.¹⁸

In addition to the Mo and Eo numbers, in the literature, one often encounters two other dimensionless quantities:

$$N_f = \frac{\rho D \sqrt{gD}}{\mu} \quad (5a)$$

and

$$Ca = \frac{\mu}{\sigma} (U_B - \bar{U}) \quad (5b)$$

The first of these quantities (N_f , which is sometimes designated as the Galilei number) has the physical significance of a Reynolds number that is based on the characteristic velocity, which is denoted as $(gD)^{1/2}$, whereas the second parameter is a measure of the relative importance of viscous and surface tension effects; in writing this latter quantity, we have anticipated the possibility of a bubble rising in a flowing liquid for which $\bar{U} \neq 0$, which is a case that will be considered in a later section. In terms of a Froude number (Fr), which is defined by

$$Fr = \frac{U_B - \bar{U}}{\sqrt{gD}} \quad (6)$$

and using the previously defined dimensionless quantities, we find

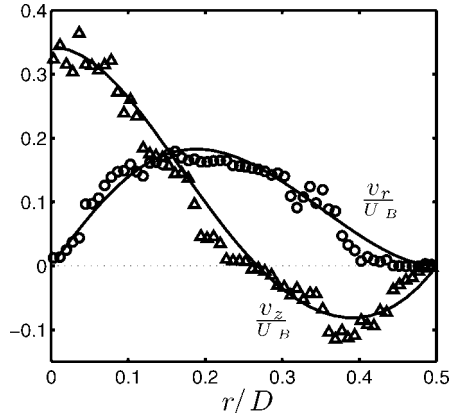


Figure 4. Axial and radial components of velocity above the bubble at $z/D = 0.111$. The symbols are the PIV measurements from ref 7, and the lines represent the present simulation results.

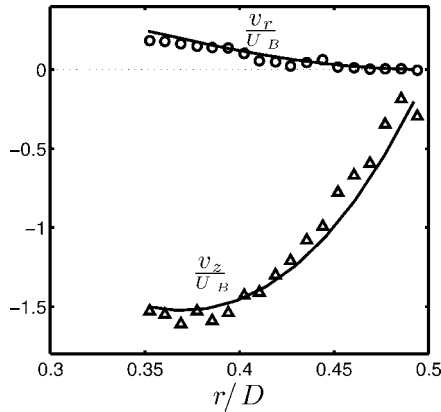


Figure 5. Axial and radial components of velocity at a height in the transition region between the bubble nose and the liquid film of $z/D = -0.504$. The symbols are the PIV measurements from ref 7, and the lines represent the present simulation results.

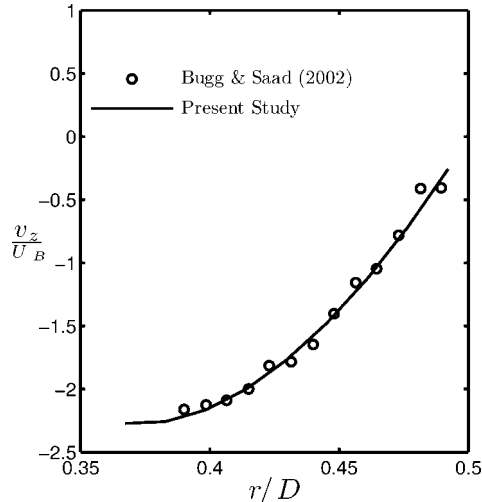


Figure 6. Axial velocity profile in the fully developed falling film along a rising Taylor bubble at a distance of $z/D = -2.34$ from the bubble nose. The numerical results (solid line) are compared to the PIV measurements from Bugg and Saad.⁷

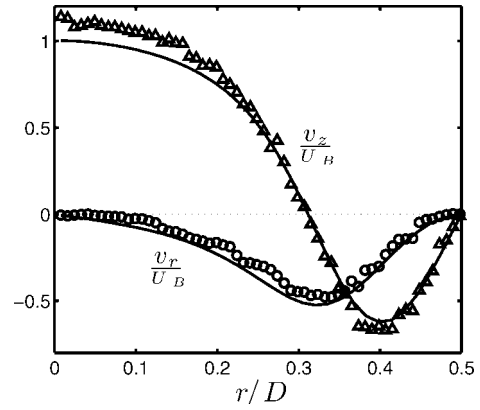


Figure 7. Axial and radial components of velocity at a distance $1/5D$ below the bubble tail. The numerical results (solid line) are compared to the PIV measurements from ref 7.

Table 2. Dimensionless Parameters N_f and Ca/Fr for the Cases Shown in Table 1

Morton number, Mo	Eötvös number, Eo	N_f^a	Ca/Fr^b
1.6×10^{-11}	14.7	3753	0.00392
1.6×10^{-11}	33	6884	0.00479
1.8×10^{-8}	15	658	0.0228
	60	1861	0.0322
4.7×10^{-5}	16.4	98.43	0.167
	18.7	25.28	0.299
1.6×10^{-2}	74.6	71.37	1.045

$$^a N_f = \rho(gD^3)^{1/2}/\mu, \quad ^b Ca/Fr = \mu(gD)^{1/2}/\sigma.$$

$$N_f = \left(\frac{Eo^3}{Mo} \right)^{1/4} \quad (7a)$$

$$Ca = (EoMo)^{1/4} Fr \quad (7b)$$

To facilitate comparison with other work, we show, in Table 2, the values of these numbers in correspondence with those shown in Table 1. Inertial effects are usually assumed to dominate when $N_f > 300$ (see, for example, ref 2), which is found to be true for all but the two largest Mo cases. Because Fr is typically on the order of 0.1, the capillary number will be primarily small.

In most of the examples, we consider a spatial period $L/D = 6$ and bubbles with an equivalent length $H/D = 1.5$; here, H is defined as the length of pipe that the gas would occupy if it completely filled the cross section. With these choices, the volume fraction occupied by the gas in the periodic cell is 25%. In all the cases that follow, we used square cells with 35 equally spaced nodes in the radial direction. Numerical convergence tests showed that this level of discretization was adequate to resolve the flow.

Figure 8 shows the shapes of steadily rising bubbles and the corresponding streamlines for a low-viscosity case ($Mo = 1.8 \times 10^{-8}$, with $Eo = 15$ and 60) and for a high-viscosity case ($Mo = 1.6 \times 10^{-2}$ with $Eo = 18.7$ and 74.6). The frame of reference is the rest frame of the bubble. The calculated rising velocities for these cases, as well as other cases, are shown in the last column of Table 1 and are found to be within $\pm 1\%$ of the measured velocities in Figure 2 in the work by White and Beardmore,¹⁸ who experimented with single bubbles in tubes that were closed at both ends. The excellent agreement with these experimental results indicates that the finite length of the computational cell and the artificial periodicity that it implies have a negligible effect on the present results. One may conclude that the bubbles only affect the flow in their immediate vicinity.

For the low-viscosity case, a strong recirculating eddy forms behind the bubble; the flow does not separate for the high-

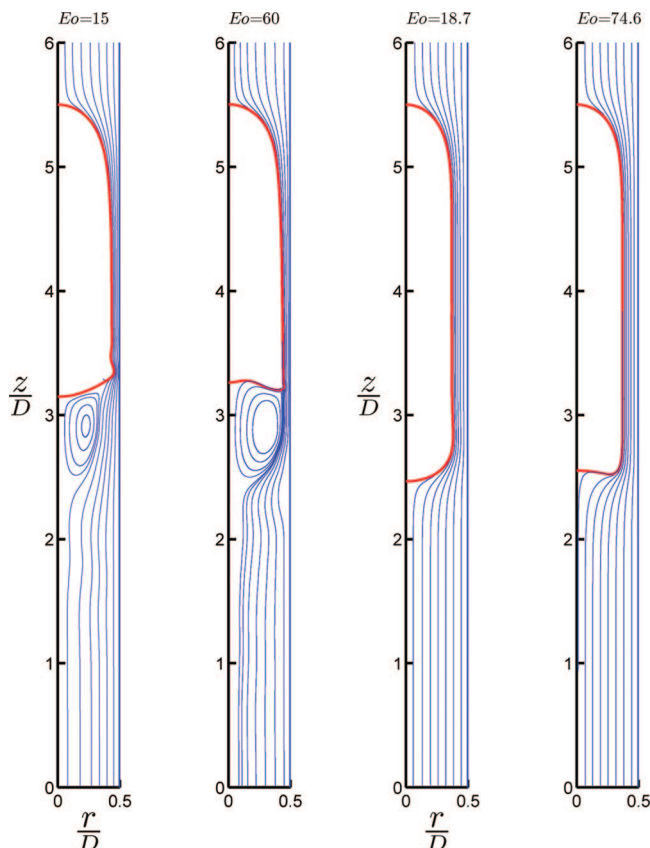


Figure 8. Streamlines around a Taylor bubble rising in a stagnant liquid in the bubble rest frame. The first two examples are for a low-viscosity liquid with $Mo = 1.8 \times 10^{-8}$ and $Eo = 15$ and 60 , respectively. The two examples on the right are for $Mo = 1.6 \times 10^{-2}$ and $Eo = 18.7$ and 74.6 , respectively.

viscosity case, as expected. It is also interesting to note the reversal of the curvature of the bubble bottom as the surface tension effects decrease with increasing Eo . We will revisit this point later.

An interesting phenomenon that has been reported in the literature (see, e.g., the works of Bretherton,¹⁹ Zukoski,²⁰ and White and Beardmore¹⁸) is that, when surface tension effects are large, the bubble remains stuck in the tube and does not rise. In agreement with Bretherton,¹⁹ White and Beardmore¹⁸ quoted a value of $Eo = 3.4$ that was necessary for this phenomenon to occur, which is similar to that reported by several authors.¹⁰ We have attempted a simulation with this Eo value and $Mo = 1.6 \times 10^{-11}$, finding that, when the bubble is released from its initial shape, its lateral surface gets closer and closer to the tube walls until the calculation fails. This result suggests that, in an attempt to reduce its surface energy, the bubble tries to approach a sphere until, presumably, the liquid film breaks and gas–liquid–solid contact lines form, which prevent further motion.

When viscous effects are not too strong, the bubble tail may oscillate long after a steady velocity has been reached. This is the case, for example, for the first example in Figure 8, $Eo = 15$ (the only bubble with an oscillating tail in this figure). The bubble tail is found to oscillate periodically, as shown in Figure 9 by several traces over a period of time of approximately $(D/g)^{1/2}$. The frequency of the oscillation is $\sim 1.10 (g/D)^{1/2}$. The unsteadiness is confined to this region as the bubble nose and lateral film surface are smooth and steady. The frequency f of these oscillations can be estimated using the theory of gravity–capillary waves, according to which

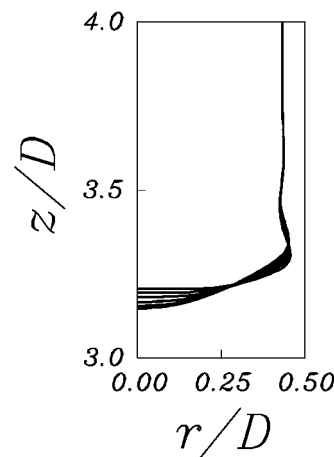


Figure 9. Example of an oscillating bubble bottom, with $Eo = 15$, $Mo = 1.8 \times 10^{-8}$. The traces are taken over a period of time of approximately $(D/g)^{1/2}$.

$$f = \frac{1}{2\pi} \sqrt{gk + \left(\frac{\sigma}{\rho}\right)k^3} \quad (8)$$

in which k is the wavenumber. For the lowest mode of standing waves in a tube, $k = k_1^0/(D/2)$, where k_1^0 is the first zero of $J_0' = 0$ ($k_1^0 \approx 3.832$). With this estimate, we find

$$f\sqrt{\frac{D}{g}} = \frac{1}{2\pi} \sqrt{2k_1^0 + \frac{8}{Eo}(k_1^0)^3} \approx 0.441 \sqrt{1 + \frac{58.7}{Eo}} \quad (9)$$

which, for $Eo = 15$, gives the dimensionless frequency $f(D/g)^{1/2} \approx 0.98$. If the diameter of the bubble bottom is estimated more closely as $D_b \approx 0.9D$, so that k in eq 8 becomes $k = k_1^0/(0.9D/2)$, the dimensionless frequency takes the value $f(D/g)^{1/2} \approx 1.12$, in better agreement with the numerical value of 1.10.

As surface tension effects decrease, several other local unsteady effects develop, even with relatively high liquid viscosities. An example would be the appearance of waves on the falling film at the bubble sides. Figure 10, for $Mo = 1.5 \times 10^{-3}$, $Eo = 100$, and a spatial period of $L/D = 4$ shows several free surface profiles over a time interval of $\sim (D/g)^{1/2}$. These waves have recently been studied by Liberzon et al.²¹

Figure 11 shows another form of local unsteadiness. In this case, viscous effects are relatively strong and $Mo = 3.6 \times 10^{-4}$, but the Eötvös number is large ($Eo = 300$), so that surface tension effects are weak. It is observed that a gas film is pulled down along the outer perimeter of the bubble tail. With the present method, we cannot resolve the evolution of this structure further, although its unsteady nature suggests that it will eventually detach from the main gas volume and break into many small bubbles, because of its high surface energy.

By exploring the parameter space (Eo, Mo) with $L/D = 4$, we find three regions with steady, wavy, and tail-unstable bubbles, as shown in Figure 12. At high Eo values, the bubble develops an unsteady skirt, similar to that shown in Figure 11; the minimum Eo value for this behavior increases as the Mo value increases. For large Mo values and small to moderate Eo values, the bubble rises and maintains a steady shape. Between these two regimes, waves develop along the film. A check of the flow structure shows that the interaction between successive bubbles can be neglected in the parameter range shown.

Rise in a Flowing Liquid

Slug flow is most frequently encountered in a flowing system, and, therefore, it is interesting to consider the rise of Taylor

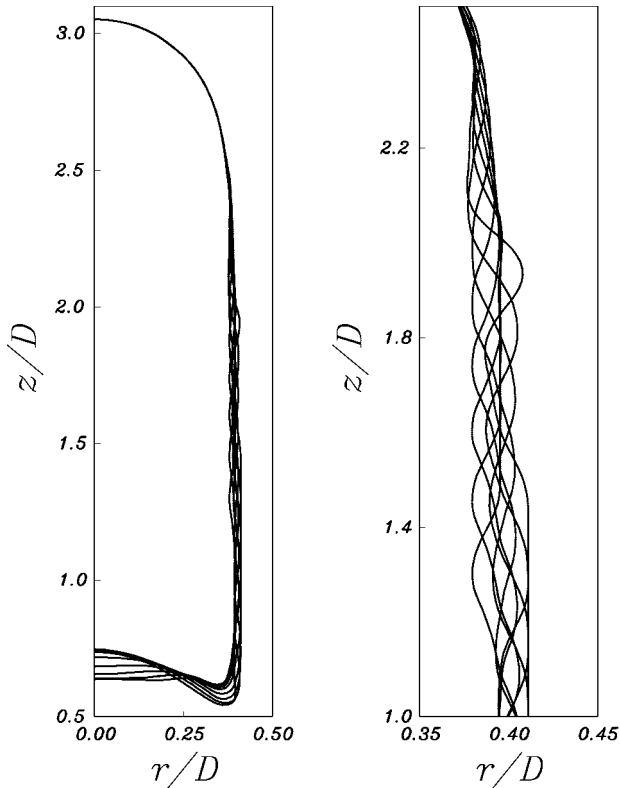


Figure 10. Local unsteady behavior of a rising Taylor bubble for $Mo = 1.5 \times 10^{-3}$, $Eo = 100$, and $L/D = 4$. The figure on the right shows details of the waves on the falling film.

bubbles in a flowing liquid. Some examples are shown in Figures 13 and 14, in which \bar{U} denotes the volumetric flux, which is equal to the cross-sectional average of the liquid velocity away from the bubble. Again, we used equal square cells with 35 nodes in the radial direction; the computational domain had a length of 6 tube diameters.

Figure 13 depicts a low-viscosity case, with $Mo = 1.8 \times 10^{-8}$, $Eo = 15$, and liquid velocities of $\bar{U}/(gD)^{1/2} = 0, 0.15$, and 0.76 . As noted previously, the frame of reference is the rest frame of the bubble. As the incoming liquid velocity increases, the detached eddy behind the bubble increases in length until it occupies the entire computational domain and interacts with the succeeding bubble. Because of volume conservation, the liquid that forms the film between the bubble and the wall has a higher velocity than the liquid behind the bubble. The effect is similar to an annular jet entering a liquid pool. As \bar{U} increases, the bubble rises faster and the velocity of this jet correspondingly increases and affects a longer and longer portion of the following liquid slug. Thus, successive bubbles spaced in such a way that they would not interact in a quiescent liquid might begin to interact in a flowing liquid. This observation suggests that, for example, a steady slug flow regime at one flow rate might be drastically changed by an increase in the flow rate. Simulations for high-viscosity cases show that this effect is greatly decreased at larger Mo values.

Figure 14 depicts a moderate viscosity case, with $Mo = 4.7 \times 10^{-5}$, $Eo = 16.4$, and $\bar{U}/(gD)^{1/2} = -0.41, -0.2, 0, 0.2$, and 1 . Here, too, the wake extends as the incoming velocity increases, more so with a downward velocity than with an upward velocity.

The experiments of ref 23 show that, for a single Taylor bubble rising in an upward flowing liquid, the measured bubble rising velocity is well-fitted by

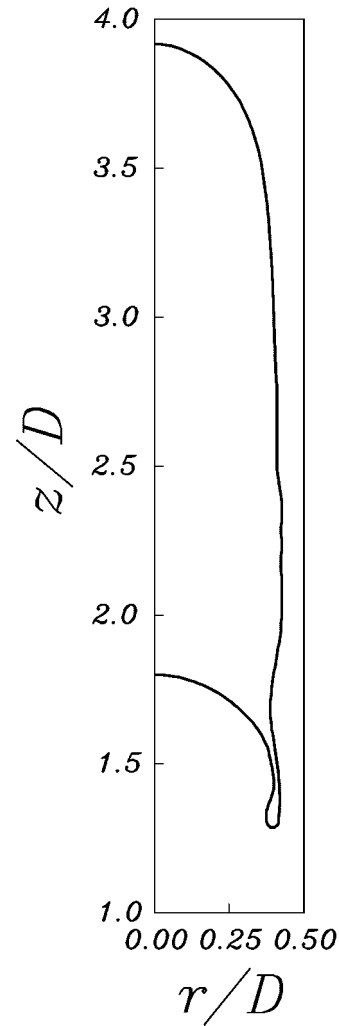


Figure 11. Snapshot of a Taylor bubble in the process of developing a gas "skirt" due to weak surface-tension effects, with $Mo = 3.6 \times 10^{-4}$ and $Eo = 300$.

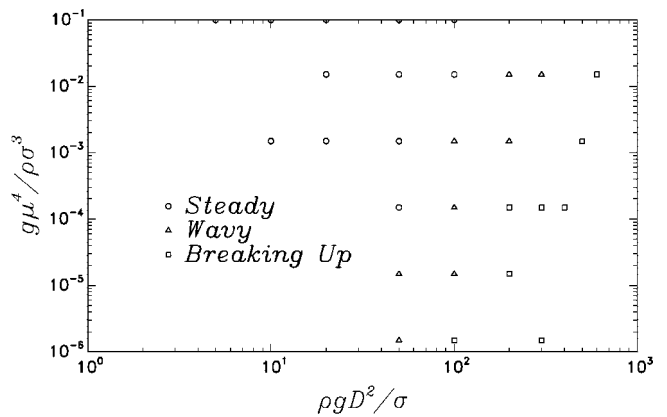


Figure 12. Phase diagram of the behavior of a bubble rising in quiescent fluid with $L/D = 4$.

$$U_B = C\bar{U} + U_0 \quad (10)$$

where U_0 is the bubble rising velocity in a stagnant liquid and the constant C is dependent on the velocity profile in the liquid ahead of the bubble and on Eo . Bendiksen²⁵ has provided an approximate form for the dependence on Eo that is applicable for fully developed laminar flow ahead of the bubble:

$$C = 2.29 \left\{ 1 - \frac{20}{Eo} [1 - \exp(-0.0125Eo)] \right\} \quad (11)$$

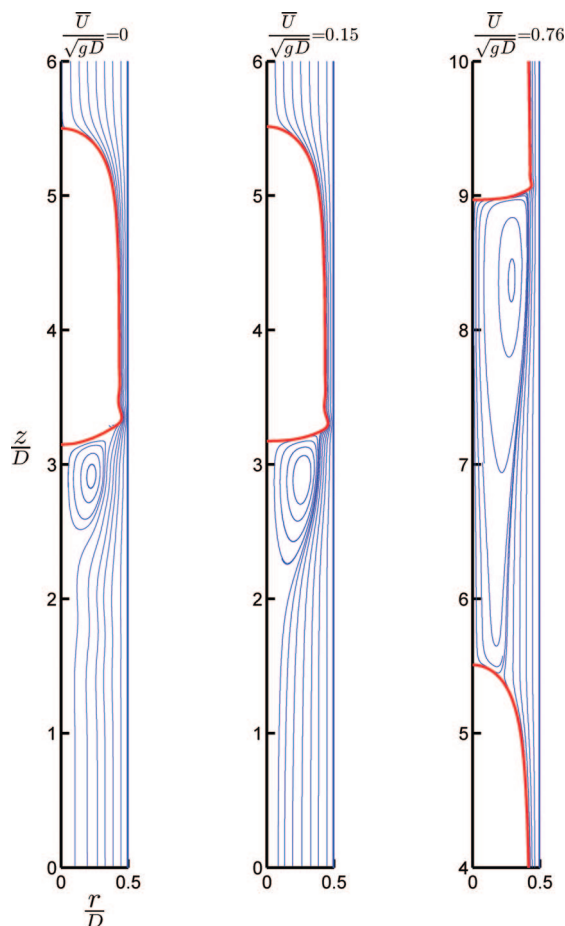


Figure 13. Streamlines around a Taylor bubble rising in an upward flowing liquid for $Mo = 1.8 \times 10^{-8}$ and $Eo = 15$ in the bubble rest frame. The values of the liquid mean velocity (or total volumetric flux) are $\bar{U}/(gD)^{1/2} = 0, 0.15$, and 0.76 . The bubble rising velocities are computed to be $U_B/(gD)^{1/2} = 0.23, 0.42$, and 1.26 , respectively.

For both $Eo = 15$ and $Eo = 16.4$, this equation gives essentially the same result: $C \approx 1.77$. A detailed study of the dependence of C on the flow conditions has recently been published by Ha-Ngoc and Fabre.²⁶

Our numerical results for $(U_B - U_0)/(gD)^{1/2}$ in a flowing liquid are shown in Figure 15, where the line defined by eq 10 is also shown; for U_0 , we use our calculated results for the rising velocity in a stagnant liquid. The results agree with the relation described by eq 10 only for low or moderate liquid velocities, as could have been anticipated from the observed lengthening of the wake with increasing liquid velocity. One notices in this figure that the interaction between successive bubbles leads to a decrease of the rising velocity for upflow, and to a slight increase in downflow.

Returning to Figure 14 for the moderate viscosity case, we note that, for upward liquid flow, the closed wake behind the bubble is primarily localized near the bubble tail and has a clockwise recirculation, in agreement with the jet picture previously outlined. In the two downward liquid flow examples shown, however, the recirculation is in the opposite direction. This feature can be understood considering the velocity of the bubble, relative to the tube wall. From eq 10, we find $U_B = 0$ for $\bar{U} = -U_0/C$, which, with the data of Figure 14, gives $\bar{U}/(gD)^{1/2} = -0.11$. For \bar{U} values that are more negative than this value, the wall is moving upward, relative to the bubble, which explains the inversion of the circulation. In any event, it is well-known that, in such downward liquid flows, bubbles have a tendency to be unstable against nonaxisymmetric perturbations

(see, e.g., refs 22–24), which is a feature that clearly cannot be reproduced in the present study; an explanation of the mechanism responsible for the instability has recently been presented in ref 27.

The bubble tail is convex to the liquid or to the gas, for high or low surface tension, respectively. An approximate criterion for a convex bubble tail can be formulated by observing that, for the tail to be convex, surface tension should be large enough to overcome the inertia effect. If one estimates the radius of curvature of the convex tail to be on the order of the tube radius $D/2$, this criterion leads to

$$\frac{2\sigma}{D/2} > \frac{1}{2}\rho(U_B - \bar{U})^2 \quad (12)$$

which may be written as $We < 8$ by introducing the Weber number:

$$We = \frac{\rho(U_B - \bar{U})^2 D}{\sigma} \quad (13)$$

Table 3 lists the We values for several cases that we have simulated. It is observed that a We criterion seems to be reasonable, although it seems that a value closer to $We \approx 5$ may be more appropriate than $We = 8$. This difference is not surprising, given the approximate argument leading to eq 12. Based on their numerical simulations in a quiescent liquid, Bugg et al.⁶ formulated an analogous criterion in terms of the Froude number: $Fr \equiv U_B/(gD)^{1/2} > 0.3$. It can be seen in this table (where, for a flowing liquid, the Froude number is defined as $Fr = (U_B - \bar{U})/(gD)^{1/2}$) that this criterion does not seem to perform as well as that based on We .

The shapes of the bubble nose for various liquid flow rates and $Mo = 4.7 \times 10^{-5}$ and $Eo = 16.4$ are compared in Figure 16. As the liquid velocity increases, the relative velocity $U_B - \bar{U}$ increases, as does the curvature of the nose. As shown in ref 27, this fact has important consequences on the axial stability of Taylor bubbles. A similar comparison for the bubble tails is shown in Figure 17. As the liquid velocity increases, the value of We also increases and the tail becomes flatter. For the highest velocity case, $\bar{U}/(gD)^{1/2} = 1$, the bubble-liquid relative velocity is so large that the bubble is considerably stretched and the liquid film along its sides is thicker.

Sudden Expansion

Experiments show that the velocity of a steadily rising bubble is independent of the bubble length as long as the bubble is long enough (about twice the tube diameter or more). Thus, if a Taylor bubble expands because of a reduction of the ambient pressure, its final steady-state velocity should be the same as that before the expansion. Here, we show some results on the transient behavior between the initial and final steady states.

It is well-known that the steady rising velocity of a bubble is strongly influenced by the liquid velocity distribution near its nose (see, for example, refs 23, 28, and 29). If we consider a situation in which the tube top is closed and the expansion is due to a lowering of the pressure at the tube bottom, one would expect hardly any effect on the bubble rising velocity (taken as the velocity of the bubble nose). In contrast, if the tube bottom is closed and the expansion occurs above the bubble, the bubble will effectively be rising in a moving liquid and, therefore, we expect a strong effect on the rising velocity during the transient.

To study this phenomenon, we first perform a simulation to steady state. We then restart the calculation using a finite domain, rather than periodicity, imposing zero liquid velocity on the upper boundary, when the lower pressure falls, or on

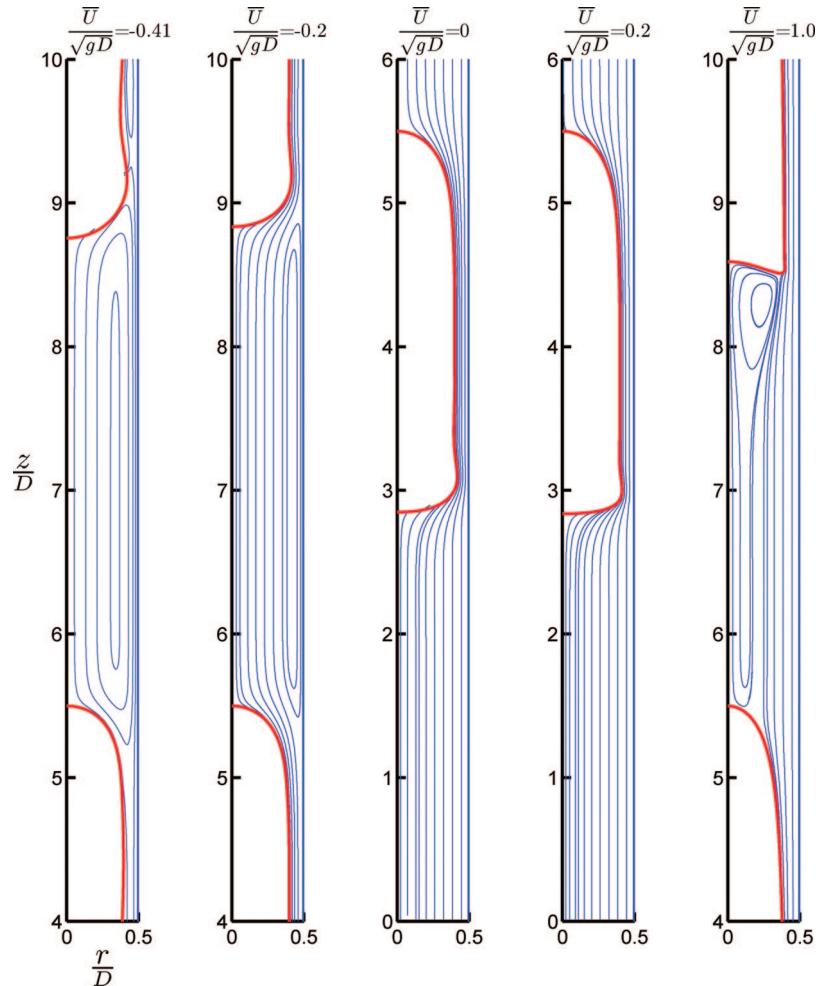


Figure 14. Streamlines around a Taylor bubble rising in an upward or downward flowing liquid for $Mo = 4.7 \times 10^{-5}$, $Eo = 16.4$ in the bubble rest frame. The values of the liquid mean velocities are $\bar{U}/(gD)^{1/2} = -0.41, -0.2, 0, 0.2$, and 1 . The bubble rising velocities are computed to be $U_B/(gD)^{1/2} = -0.44, -0.12, 0.19, 0.50$, and 1.88 , respectively. For upward liquid flow, recirculation in the closed wake is a clockwise recirculation. In the two downward liquid flow examples, recirculation is in the opposite direction, because the wall is moving upward, relative to the bubble.

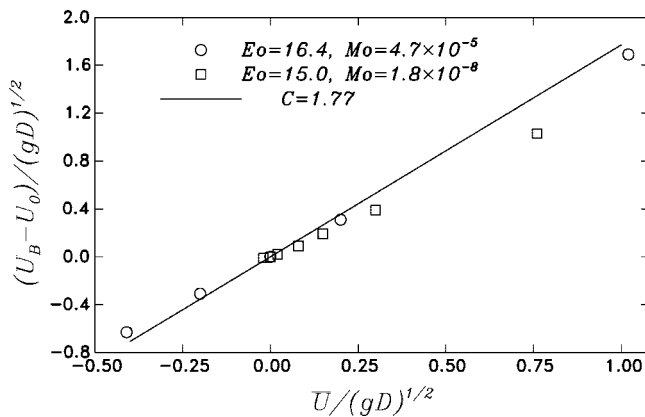


Figure 15. Bubble rising velocity in flowing liquid. The points are the results from numerical simulation, and the line represents eq 10 ($U_B = CU + U_0$).

the lower boundary in the opposite case. On the other boundary, the desired P is imposed and the normal gradients of the velocity components are set to zero. The length L of the computational domain is $L/D = 8$, with square cells and 35 nodes in the radial direction. Because of the manner in which time is advanced (section 2), the pressure condition is always imposed at the same distance above or below the bubble. This procedure has the effect of not accounting for the gradually falling hydrostatic

pressure, which, however, is a small effect, compared to the imposed pressure change.

Let us begin with a very-high-viscosity-liquid example, with $Mo = 10$ and $Eo = 100$. Starting from steady-state conditions, the pressure at the top of the tube suddenly drops by a dimensionless amount $1/2\{\Delta p/(\rho g D) + L/D\}$, where $\Delta p/(\rho g D)$ is the calculated pressure difference between the top and bottom of the computational cell at the end of the preliminary steady calculation; the velocity is kept to zero at the bottom of the tube. The bubble is taken to expand isothermally, which determines the gas pressure p_g in the normal-stress boundary condition described by eq 1. The initial pressure is assumed to be equal to the hydrostatic pressure at the bubble center at the start of the transient calculation, and liquid flows out of the top of the computational domain.

The bubble volume change is shown in Figure 18, and the liquid cross-sectional averaged flow velocity out of the tube top is shown together with the bubble rising velocity in Figure 19. As the liquid velocity increases, so does the bubble nose velocity U_B , until it stabilizes, returning to the value it had before the expansion by the time the volume reaches its final value. A representation of the process on a (U_B, \bar{U}) plane is shown in Figure 20, where the solid line is the steady-state relation described by eq 10 with $C = 2.27$, which is the value given by eq 11 for this Eo value. For U_0 , we use the steady-state value before the expansion, which is calculated to be

Table 3. Froude (Fr) and Weber (We) Numbers and the Bubble Tail Shape in a Stagnant or Flowing Liquid

Morton number, Mo^a	Eötvös number, Eo^b	$\bar{U}/(gD)^{1/2}$	Froude number, Fr^c	Weber number, We^d	convex tail?
1.6×10^{-2}	18.7	0	0.10	0.2	yes
4.7×10^{-5}	16.4	0	0.19	0.6	yes
1.8×10^{-8}	15	0	0.23	0.8	yes
1.8×10^{-8}	15	0.15	0.27	1.1	yes
4.7×10^{-5}	16.4	0.2	0.30	1.5	yes
1.8×10^{-8}	15	0.76	0.50	3.8	yes
1.6×10^{-2}	18.7	0.40	0.51	4.9	yes
1.6×10^{-2}	74.6	0	0.27	5.4	no
1.8×10^{-8}	60	0	0.33	6.5	no
1.6×10^{-2}	74.6	0.14	0.39	11.3	no
4.7×10^{-5}	16.4	1.02	0.86	12.1	no
1.6×10^{-2}	18.7	0.79	0.92	15.8	no
1.6×10^{-2}	74.6	0.28	0.52	20.2	no

^a $Mo = g\mu^4/(\rho\sigma^3)$. ^b $Eo = \rho g D^2/\sigma$. ^c $Fr = (U_B - \bar{U})/(gD)^{1/2}$. ^d $We = \rho(U_B - \bar{U})^2 D/\sigma$.

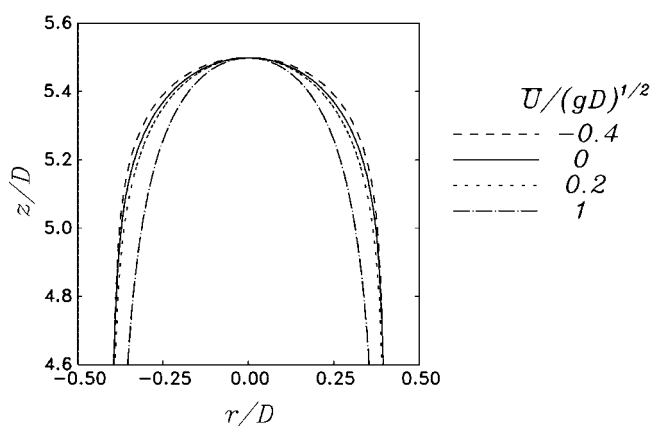


Figure 16. Bubble nose shapes for different liquid mean velocities with $Mo = 4.7 \times 10^{-5}$ and $Eo = 16.4$. The nose becomes more pointed as the liquid velocity increases.

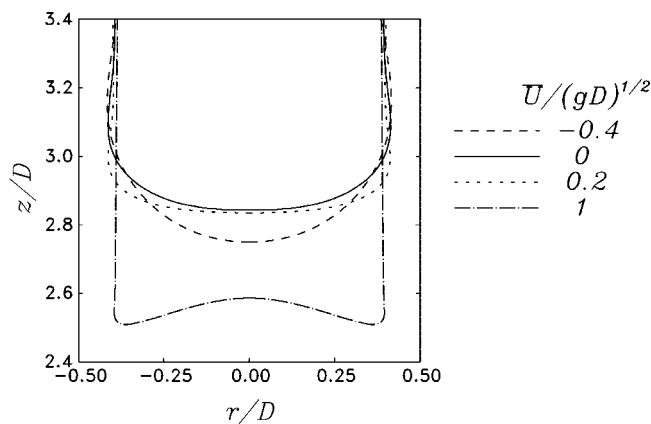


Figure 17. Bubble tail shapes for different liquid mean velocities with $Mo = 4.7 \times 10^{-5}$ and $Eo = 16.4$. As the liquid velocity increases, the bubble rises faster and the stagnation pressure behind it eventually causes the tail to become convex, relative to the gas.

$U_0 = 0.14(gD)^{1/2}$. The points in Figure 20 correspond to the calculated transient liquid and bubble velocities from Figure 19. The close agreement between the points and the line implies that the flow is in quasi-equilibrium at each instant.

The behavior is different in a lower-viscosity liquid, with $Mo = 4.7 \times 10^{-5}$ and $Eo = 16.4$. In this case, we use a smaller pressure drop, $1/5\{[\Delta p/(\rho g D)] + L/D\}$, while the velocity is kept zero at the bottom of the tube as noted previously. The bubble volume now executes damped oscillation (see Figure 21). Correspondingly, the bubble-nose and liquid velocities also oscillate (see Figure 22). The significant role of inertia in this

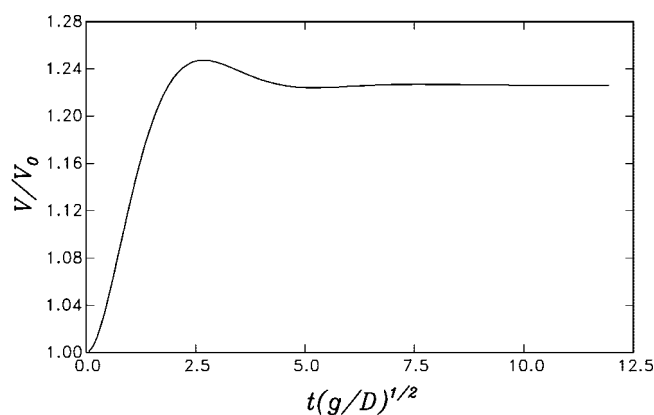


Figure 18. Bubble volume versus time after a sudden pressure drop at the top of the tube for a very viscous case ($Mo = 10$ and $Eo = 100$).

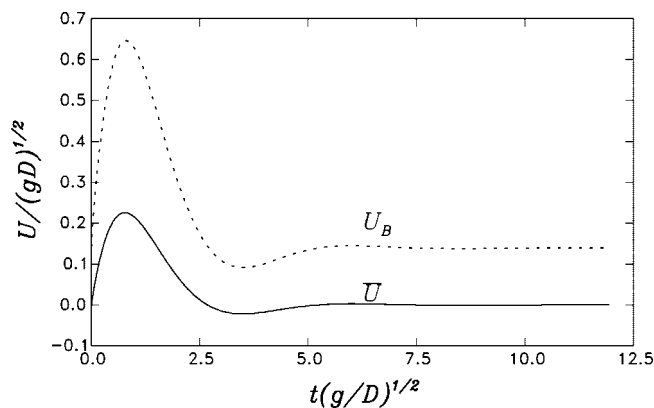


Figure 19. Bubble rising velocity and liquid mean velocity versus time after a sudden pressure drop at the top of the tube for a very viscous case ($Mo = 10$ and $Eo = 100$).

process is demonstrated by comparing the instantaneous liquid and bubble velocities with the steady-state relation described by eq 10, as shown in Figure 23. For U_0 , we use the steady-state value before the expansion, which is found to be $U_0 = 0.19(gD)^{1/2}$, and $C = 1.77$. The line represents the relationship described by eq 10, and the points correspond to the calculated transient liquid and bubble velocities taken from Figure 22. It is seen that the points describe a cycle around the steady-state line and eventually settle on it. These results agree with the behavior reported in ref 23.

We can contrast this behavior with that produced by a pressure drop at the bottom of the tube. A comparison with the behavior of Figures 18–23 is shown in Figures 24 and 25. In this case, the pressure at the bottom of the tube suddenly drops

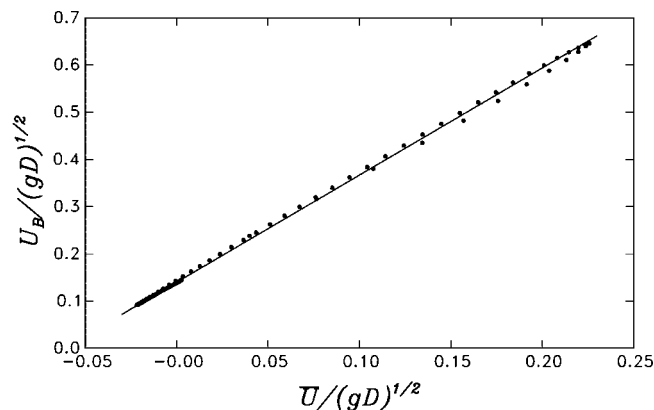


Figure 20. Velocity of the bubble nose versus liquid mean velocity for the case shown in Figures 18 and 19. The solid line is the steady-state relation that is described by eq 10 with $C = 2.27$ and $U_0 = 0.14(gD)^{1/2}$; the points represent data taken from Figure 19.

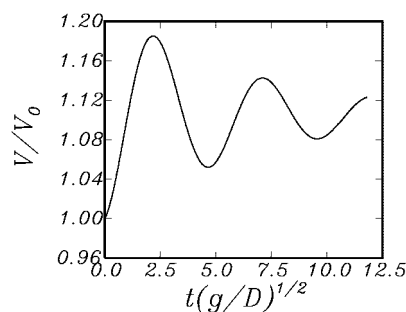


Figure 21. Bubble volume versus time after a sudden pressure drop at the top of the tube for a low-viscosity case ($Mo = 4.7 \times 10^{-5}$ and $Eo = 16.4$).

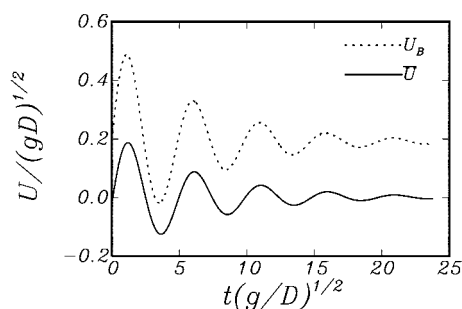


Figure 22. Bubble nose velocity and liquid mean velocity versus time after a sudden pressure drop at the top of the tube for a low-viscosity case ($Mo = 4.7 \times 10^{-5}$ and $Eo = 16.4$).

by the amount of $\frac{1}{2}[\Delta p/(\rho g D)] + L/D$. The bubble expands while liquid flows out of the tube bottom. The time dependence of the bubble volume is shown in Figure 24. The liquid average outflow velocity and the bubble nose velocity are shown in Figure 25. As the bubble expands, its rising velocity does not change, as expected and in agreement with the conclusions from ref 23.

Summary and Conclusions

In this paper, we have demonstrated the use of a finite-volume numerical method for the description of axisymmetric gas–liquid flow in the Taylor bubble regime. The computational results have been validated against some detailed measurements that are available in the literature, and the code has been used to simulate several situations of steady-state and unsteady-state flow. The results agree with the qualitative behavior of the

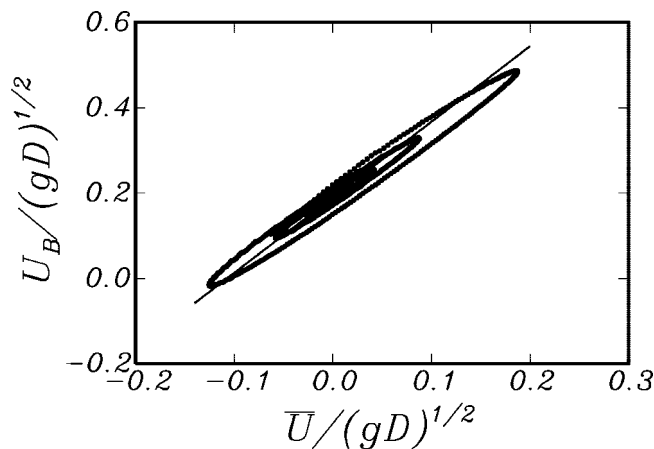


Figure 23. Bubble nose velocity versus liquid mean velocity for the cases shown in Figures 21 and 22. The solid line is the steady-state relation described by eq 10 with $C = 1.77$ and $U_0 = 0.19(gD)^{1/2}$; the points are taken from Figure 22.

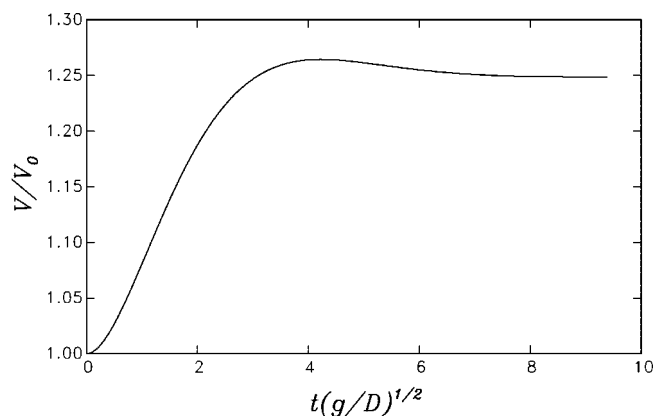


Figure 24. Bubble volume versus time after a sudden pressure drop at the bottom of the tube ($Mo = 10$ and $Eo = 100$).

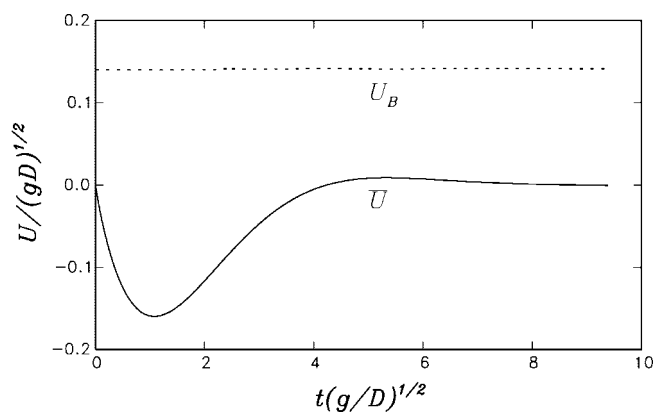


Figure 25. Bubble nose velocity and liquid mean velocity versus time after a sudden pressure drop at the bottom of the tube ($Mo = 10$ and $Eo = 100$).

systems reported in the literature, and there is also a quantitative agreement for the few quantities (mostly the rising velocity) that have been measured. The numerical results provide some interesting insight into the character of the flow, such as interaction distance, recirculating eddies, unsteady behavior, and others.

Acknowledgment

The senior author (A.P.) dedicates this work to Prof. Liang-Shih Fan with friendship, admiration, and best wishes. Prof.

Fan's OSCAR project is one of the smartest ideas senior author A.P. has ever come across! This study was supported by NASA (under Grant No. NNC05GA47G).

Literature Cited

- (1) Taitel, Y.; Barnea, D. Two-phase slug flow. In *Advances in Heat Transfer*, Volume 20; Hartnett, J. P., Irvine, T. F., Jr., Eds.; Academic Press: 1990; pp 83–132.
- (2) Fabre, J.; Liné, A. Modeling of two-phase slug flow. *Ann. Rev. Fluid Mech.* **1992**, *24*, 21–46.
- (3) Funada, T.; Joseph, D. D.; Maehara, T.; Yamashita, S. Ellipsoidal model of the rise of a Taylor bubble in a round tube. *Int. J. Multiphase Flow* **2005**, *31*, 473–491.
- (4) Mao, Z. S.; Dukler, A. E. The motion of Taylor bubbles in vertical tubes. I. A numerical simulation for the shape and rise velocity of Taylor bubbles in stagnant and flowing liquid. *J. Comput. Phys.* **1990**, *91*, 132–160.
- (5) Tomiyama, A.; Sou, A.; Sakaguchi, T. Numerical simulation of a Taylor bubble in a stagnant liquid inside a vertical pipe. *JSME Int. J.* **1996**, *B39*, 517–524.
- (6) Bugg, J. D.; Mack, K.; Rezkallah, K. S. A numerical model of Taylor bubbles rising through stagnant liquids in vertical tubes. *Int. J. Multiphase Flow* **1998**, *24*, 271–281.
- (7) Bugg, J. D.; Saad, G. A. The velocity field around a Taylor bubble rising in a stagnant viscous fluid: Numerical and experimental results. *Int. J. Multiphase Flow* **2002**, *28*, 791–803.
- (8) Son, G. A numerical method for incompressible two-phase flows with open or periodic boundaries. *Numer. Heat Transfer, Part B* **2001**, *B39*, 45–60.
- (9) Anglart, H.; Podowski, M. Z. Fluid mechanics of Taylor bubbles and slug flows in vertical channels. *Nucl. Sci. Eng.* **2002**, *140*, 165–171.
- (10) Taha, T.; Cui, Z. F. CFD modelling of slug flow in vertical tubes. *Chem. Eng. Sci.* **2006**, *61*, 676–687.
- (11) Wallis, G. W. *One-Dimensional Two-Phase Flow*. McGraw–Hill: New York, 1969.
- (12) Popinet, S.; Zaleski, S. Bubble collapse near a solid boundary: a numerical study of the influence of viscosity. *J. Fluid Mech.* **2002**, *464*, 137–163.
- (13) Lu, X. Numerical Simulation and Axial Stability Analysis of Vertical Slug Flow, Ph.D. Thesis, Johns Hopkins University, Baltimore, MD, 2006.
- (14) Press, W. H.; Vetterling, W. T.; Teukolsky, S. A.; Flannery, B. P. *Numerical Recipes in C*; Cambridge U.P.: Cambridge, U.K., 1997.
- (15) Farin, G. *Curves and Surfaces for Computer-Aided Geometric Design: A Practical Guide*; Academic Press: San Diego, CA, 2002.
- (16) Plesset, M. S.; Prosperetti, A. Bubble dynamics and cavitation. *Annu. Rev. Fluid Mech.* **1977**, *9*, 145–185.
- (17) Brown, R. A. S. The mechanics of large bubbles in tubes. I. Bubble velocities in stagnant liquids. *Can. J. Chem. Eng.* **1965**, *43*, 217–223.
- (18) White, E. T.; Beardmore, R. H. The velocity of rise of single cylindrical air bubbles through liquids contained in vertical tubes. *Chem. Eng. Sci.* **1962**, *17*, 351–361.
- (19) Bretherton, F. P. The motion of long bubbles in tubes. *J. Fluid Mech.* **1961**, *10*, 166–188.
- (20) Zukoski, E. E. Influence of viscosity, surface tension, and inclination angle on motion of long bubbles in closed tubes. *J. Fluid Mech.* **1966**, *25*, 821–837.
- (21) Liberzon, D.; Shemer, L.; Barnea, D. Upward-propagating capillary waves on the surface of short Taylor bubbles. *Phys. Fluids* **2006**, *18*, 048103.
- (22) Griffith, P.; Wallis, G. B. Two-phase slug flow. *J. Heat Transfer* **1961**, *83*, 307–320.
- (23) Nicklin, D. J.; Wilkes, J. O.; Davidson, J. F. Two-phase flow in vertical tubes. *Trans. Inst. Chem. Eng.* **1962**, *40*, 61–68.
- (24) Bendiksen, K. H. An experimental investigation of the motion of long bubbles in inclined tubes. *Int. J. Multiphase Flow* **1984**, *10*, 467–483.
- (25) Bendiksen, K. H. On the motion of long bubbles in vertical tubes. *Int. J. Multiphase Flow* **1985**, *11*, 797–812.
- (26) Ha-Ngoc, H.; Fabre, J. Test-case No. 29B: The velocity and shape of 2D long bubbles in inclined channels or in vertical tubes. *Multiphase Sci. Technol.* **2004**, *16*, 191–206.
- (27) Lu, X.; Prosperetti, A. Axial stability of Taylor bubbles. *J. Fluid Mech.* **2007**, *568*, 173–192.
- (28) Collins, R.; De Moraes, F. F.; Davidson, J. F.; Harrison, D. The motion of a large gas bubble rising through liquid flowing in a tube. *J. Fluid Mech.* **1978**, *89*, 497–514.
- (29) Polonsky, S.; Shemer, L.; Barnea, D. The relation between the Taylor bubble motion and the velocity field ahead of it. *Int. J. Multiphase Flow* **1999**, *25*, 957–975.

Received for review February 4, 2008

Revised manuscript received July 3, 2008

Accepted July 8, 2008

IE800201X